Supplementary Information

Efficient Modeling of Tapered Photonic Structures

Konrad Tschernig[1], Swati Bhargava[1], Vinzenz Zimmermann[1],
Daniel Cruz-Delgado[1], Sergio Leon-Saval[2], Stephen Eikenberry[1],
Rodrigo Amezcua-Correa[1], Miguel A. Bandres[1]

[1]CREOL, The College of Optics and Photonics, University of Central Florida, FL, USA.
[2]Institute of Photonics and Optical Science, School of Physics, University of Sydney,
NSW, Australia.

1 Modeling Light Propagation in Tapered Optical Structures

The propagation of light in weakly guiding dielectric structures, i.e. when the refractive index contrast is low, is described in very good approximation by the paraxial wave equation

$$i\partial_z\psi = -\frac{1}{2k_0}\nabla_\perp^2\psi - \frac{k_0}{2n_0^2}(n(x,y,z)^2 - n_0^2)\psi, \tag{1}$$

where $\psi(x,y,z)$ is the paraxial light field, z the propagation distance, (x,y) the transverse coordinates, $\nabla_\perp^2 = \partial_x^2 + \partial_y^2$ is the transverse Laplacian operator, $k_0 = kn_0$, $k = 2\pi/\lambda$ is the wavenumber, n_0 the reference refractive index, λ the vacuum wavelength and $n(x,y,z)$ is the refractive index distribution, which gives rise to the optical potential. In particular we are considering tapered optical potentials, where the z-dependence of $n(x,y,z)$ originates from a taper such that it shrinks or grows, without any other deformations, along the z-direction. Such a behavior is described by the taper function $\alpha(z)$, which describes the amount by which the potential has shrunk, $\alpha(z) < 1$, or grown, $\alpha(z) > 1$, compared to the initial size, $\alpha(0) = 1$ at $z = 0$. In general, the potential at the initial and any later propagation distance will differ

$$n(x,y,z) \neq n(x,y,0). \tag{2}$$

However, when we evaluate the refractive index at the *tapered position* $(\alpha(z)x, \alpha(z)y, z)$, then we obtain the same refractive index as at the initial position $(x,y,0)$

$$n(\alpha(z)x, \alpha(z)y, z) = n(x,y,0). \tag{3}$$

In order to exploit this convenient property of Eq. (3) we introduce tapered coordinates (u,v,s) via

$$(x,y,z) = (\alpha(s)u, \alpha(s)v, s)\,, \tag{4}$$

where we require $\infty > \alpha(z) > 0$ to avoid nonphysical singularities. Crucially, in this new taper reference frame, the potential is rendered z(or s)-independent

$$n(x, y, z) = n(\alpha(s)u, \alpha(s)v, s) = n(u, v, 0). \tag{5}$$

This is an appealing property, since we only need to evaluate the refractive index distribution once, when solving the paraxial equation numerically in (u, v, s) coordinates. This provides a significant advantage whenever the evaluation of the refractive index distribution is computationally costly. This is the case for multi-core photonic lanterns, which may necessitate, for example, the evaluation of multiple 2D super-Gaussian functions on a large numerical grid. Furthermore, the spatial resolution of the potential on the transverse numerical (u, v) grid remains constant, in stark contrast to standard methods where resolution decreases as the potential shrinks.

But before we can reap these advantages, we must first fully express the paraxial equation in the new coordinates. As a consequence we will obtain additional terms due to the change of coordinates. Later on we will show that these new terms can be dealt with in a numerically efficient way. We first transform the Laplacian with respect to x and y

$$\frac{\mathrm{d}\psi(u,v,s)}{\mathrm{d}x} = \frac{\partial\psi}{\partial u}\underbrace{\frac{\partial u}{\partial x}}_{=1/\alpha} + \frac{\partial\psi}{\partial v}\underbrace{\frac{\partial v}{\partial x}}_{=0} + \frac{\partial\psi}{\partial s}\underbrace{\frac{\partial s}{\partial x}}_{=0} = \frac{1}{\alpha}\frac{\partial\psi}{\partial u} \tag{6}$$

$$\Rightarrow \frac{\mathrm{d}^2\psi}{\mathrm{d}x^2} = \frac{1}{\alpha^2}\frac{\partial^2\psi}{\partial u^2} \quad \text{and} \quad \frac{\mathrm{d}^2\psi}{\mathrm{d}y^2} = \frac{1}{\alpha^2}\frac{\partial^2\psi}{\partial v^2}. \tag{7}$$

From the z-derivative we obtain two additional terms

$$\begin{aligned}
\frac{\mathrm{d}\psi(u,v,s)}{\mathrm{d}z} &= \frac{\partial\psi}{\partial u}\underbrace{\frac{\partial u}{\partial z}}_{=-\frac{x\dot\alpha}{\alpha^2}} + \frac{\partial\psi}{\partial v}\underbrace{\frac{\partial v}{\partial z}}_{=-\frac{y\dot\alpha}{\alpha^2}} + \frac{\partial\psi}{\partial s}\underbrace{\frac{\partial s}{\partial z}}_{=1} && (8)\\
&= -\frac{u\dot\alpha}{\alpha}\frac{\partial\psi}{\partial u} - \frac{v\dot\alpha}{\alpha}\frac{\partial\psi}{\partial v} + \frac{\partial\psi}{\partial s} && (9)\\
&= -\frac{\dot\alpha}{\alpha}\left(u\frac{\partial\psi}{\partial u} + v\frac{\partial\psi}{\partial v}\right) + \frac{\partial\psi}{\partial s}, && (10)
\end{aligned}$$

where $\dot\alpha = \partial\alpha/\partial s$. We arrive at the tapered paraxial wave equation

$$i\partial_s\psi = -\left(\frac{1}{2k_0\alpha(s)^2}\right)\nabla^2_{u,v}\psi - i\left(-\frac{\dot\alpha(s)}{\alpha(s)}\right)(u\partial_u + v\partial_v)\,\psi - \frac{k_0}{2n_0^2}(n(u,v,0)^2 - n_0^2)\psi, \tag{11}$$

where the potential is now static, in other words, only a function of the transverse tapered coordinates u, v. However, we obtain two modifications with respect to the usual paraxial wave equation. Firstly, we have obtained the additional term $i\dot\alpha(s)/\alpha(s)\,(u\partial_u + v\partial_v)\,\psi$ and, secondly, the Laplacian $-\nabla^2_{u,v}/(2k_0\alpha(s)^2)\psi$ is now s-dependent. The s-dependence of the Laplacian may be interpreted as an s-dependent (effective) wave number $k(s) = k_0\alpha(s)^2$ of the incident light, which grows and shrinks while the potential remains static. The additional term contains the expression $u\partial_u + v\partial_v$ and is, for this reason, quite problematic at first sight. Since it is neither diagonal in real space (u, v) nor in Fourier space (k_u, k_v), it is intractable with conventional Fourier propagation methods. However, as we will see shortly, this term is akin to an artificial gauge field and we will be able to remove it with a suitable gauge transformation.

2 Tapered Paraxial Equation in 1D

In the previous section we have obtained an additional term in the taper reference frame, which rendered the paraxial equation intractable with the usual Fourier methods. In this section we will show that the additional term is equivalent to an artificial gauge field. For the sake of simplicity we will first consider the 1D tapered paraxial equation

$$i\partial_s\psi = -\left(\frac{1}{2k_0\alpha(s)^2}\right)\partial_u^2\psi - i\left(-\frac{\dot{\alpha}(s)}{\alpha(s)}\right)u\partial_u\psi + V_0(u)\psi, \tag{12}$$

where we have defined $V_0(u) = -\frac{k_0}{2n_0^2}(n(u,0)^2 - n_0^2)$. By using $u\partial_u = \partial_u u - 1$ and omitting the s-dependence for clarity, we rewrite

$$i\partial_s\psi = -\left(\frac{1}{2k_0\alpha^2}\right)\partial_u^2\psi - i\left(-\frac{1}{2}\frac{\dot{\alpha}}{\alpha}\right)(u\partial_u + \partial_u u)\psi - \frac{i}{2}\frac{\dot{\alpha}}{\alpha}\psi + V_0\psi. \tag{13}$$

We can eliminate the term $-i\dot{\alpha}/(2\alpha)\psi$ by performing an amplitude scaling transformation. To do so, we define the new field $\phi(u,v,s)$ via

$$\psi(u,v,s) = \exp\left(-\frac{1}{2}\int_0^s \frac{\dot{\alpha}(s')}{\alpha(s')}\mathrm{d}s'\right)\phi(u,v,s) \tag{14}$$

$$= \exp\left(-\frac{1}{2}\log(\alpha(s))\right)\phi \tag{15}$$

$$= \frac{1}{\sqrt{\alpha}}\phi. \tag{16}$$

Thus, the left-hand side of Eq. (13) transforms to

$$i\partial_s\psi = i\frac{1}{\sqrt{\alpha}}\partial_s\phi - \frac{i}{2}\alpha^{-3/2}\dot{\alpha}\phi = i\frac{1}{\sqrt{\alpha}}\partial_s\phi - \frac{i}{2}\frac{\dot{\alpha}}{\alpha}\psi. \tag{17}$$

Now the term $-i\dot{\alpha}/(2\alpha)\psi$ is present on both sides of Eq. (13) and cancels out. After multiplying both sides with $\sqrt{\alpha}$ we are left with

$$i\partial_s\phi = -\left(\frac{1}{2k_0\alpha^2}\right)\partial_u^2\phi - i\left(-\frac{1}{2}\frac{\dot{\alpha}}{\alpha}\right)(u\partial_u + \partial_u u)\phi + V_0\phi. \tag{18}$$

In order to simplify the notation we introduce the abbreviations

$$c(s) = \frac{1}{2k_0\alpha(s)^2} \tag{19}$$

$$b(s) = -\frac{1}{2}\frac{\dot{\alpha}(s)}{\alpha(s)}. \tag{20}$$

Now we use the method of completing the square

$$i\partial_s\phi = -c(s)\left(\partial_u^2 + i\frac{b(s)}{c(s)}(u\partial_u + \partial_u u)\right)\phi + V_0\phi \tag{21}$$

$$= -c(s)\left(\left(\partial_u + i\frac{b(s)}{c(s)}u\right)^2 + \frac{b^2(s)}{c^2(s)}u^2\right)\phi + V_0\phi \tag{22}$$

$$= -c(s)\left(\partial_u + i\frac{b(s)}{c(s)}u\right)^2\phi - \frac{b^2(s)}{c(s)}u^2\phi + V_0\phi \tag{23}$$

$$= c(s)\left(i\partial_u - \frac{b(s)}{c(s)}u\right)^2\phi - \frac{b^2(s)}{c(s)}u^2\phi + V_0\phi. \tag{24}$$

By performing these transformations we were able to replace the undesirable term $u\partial_u$ in Eq. (12) with an artificial gauge field given by

$$A(u,s) = -\frac{b(s)}{c(s)}u = k_0\alpha(s)\dot{\alpha}(s)u \tag{25}$$

and an additional potential

$$V_1(u,s) = -\frac{b^2(s)}{c(s)}u^2 = -\frac{k_0}{2}\dot{\alpha}^2(s)u^2, \tag{26}$$

and the tapered paraxial wave equation acquires the new form

$$i\partial_s\phi = \frac{1}{2k_0\alpha^2}\left(i\partial_u + A(u,s)\right)^2\phi - \frac{k_0}{2}\dot{\alpha}^2(s)u^2\phi + V_0(u)\phi, \tag{27}$$

where the original field is obtained via $\psi(u,s) = \phi(u,s)/\sqrt{\alpha(s)}$.

2.1 Gauging Away the Gauge Field

In the previous section we have re-expressed the tapered paraxial wave equation and found an artificial gauge field and an extra potential. However, this formulation is still incompatible with Fourier propagation methods since the term $\left(i\partial_u + A(u,s)\right)^2$ in Eq. (27) is not diagonal in both real- and Fourier-space. But it is clear now that the tapered paraxial wave equation resembles the Schrödinger equation for a particle under the influence of a vector potential A. Furthermore, it is well-known that the Schrödinger equation is invariant under gauge transformations. This crucial realization enables us to perform a suitable gauge transformation to remove the gauge field A. This will further modify the tapered paraxial wave equation but will finally render it tractable with Fourier propagation methods.

We can now perform a gauge transformation defined by the following replacements

$$\phi(u,s) \to \Phi(u,s) = e^{i\Lambda(u,s)}\phi(u,s) \tag{28}$$

$$A \to A' = A + \partial_u\Lambda \tag{29}$$

$$V \to V' = V - \partial_s\Lambda, \tag{30}$$

where the scalar function $\Lambda(u,s)$ is yet free to choose. Since our goal is to render the new paraxial wave equation tractable with Fourier methods, we now exploit this freedom to require that the new gauge field vanishes, $A' = A + \partial_u\Lambda = 0$. This implies $A = -\partial_u\Lambda$ and we can easily find the Λ-function that fulfills our requirement

$$\Lambda(u,s) = \frac{b(s)}{2c(s)}u^2 = -\frac{k_0}{2}\alpha\dot{\alpha}u^2. \tag{31}$$

As the next step, we have to find the new modified potential $V' = V - \partial_s\Lambda$ by evaluating

$$-\partial_s\Lambda = -\frac{1}{2}u^2\partial_s\left(\frac{b(s)}{c(s)}\right) = \frac{k_0}{2}\left(\dot{\alpha}^2 + \alpha\ddot{\alpha}\right)u^2. \tag{32}$$

Quite conveniently, the extra potential we have found in the previous section, see Eq. (27), cancels with the first term in Eq. (32). This leaves us with the final form of the 1D tapered paraxial wave equation

$$i\partial_s\Phi = -\left(\frac{1}{2k_0\alpha(s)^2}\right)\partial_u^2\Phi + \left(\frac{k_0}{2}\alpha(s)\ddot{\alpha}(s)u^2 + V_0(u)\right)\Phi. \tag{33}$$

This form is finally tractable with Fourier propagation methods, since the remaining terms are diagonal in either real- or Fourier-space, respectively. The first term resembles the usual Laplacian of the standard paraxial wave equation but includes the s-dependent factor $1/\alpha(s)^2$, which can be interpreted as an s-dependent variation of the wavelength. The second term contains the static version of the tapered potential $V_0(u)$, as per construction. Lastly, we have obtained an additional harmonic oscillator u^2 potential that is proportional to the taper function and it's second derivative. Quite interestingly, this potential is rendered attractive, when $\ddot{\alpha}(s) > 0$, or repulsive, when $\ddot{\alpha}(s) < 0$. In the special case of a linear taper, $\ddot{\alpha}(s) = 0$, the extra potential vanishes exactly. Once we have solved Eq. (33), we obtain the original field via

$$\psi(u, s) = \frac{1}{\sqrt{\alpha(s)}} e^{i \frac{k_0}{2} \alpha(s) \dot{\alpha}(s) u^2} \Phi(u, s). \tag{34}$$

We emphasize that, so far, no approximation has been made and Eq. (34) solves Eq. (1) exactly, as long as $\Phi(u, s)$ is the solution of Eq. (33).

2.2 1D Fourier Propagation in the Taper Reference Frame

The task is now to solve Eq. (33) numerically, which is of the form

$$i\partial_s \Phi = \mathcal{H}(s)\Phi. \tag{35}$$

with the operators $\mathcal{H}(s) = A(s) + B(s)$, $A(s) = -\left(2k_0\alpha(s)^2\right)^{-1} \partial_u^2$ and $B(s) = k_0\alpha(s)\ddot{\alpha}(s)u^2/2 + V_0(u)$. The formal solution for a time step from s to $s + \Delta s$ is then

$$\Phi(u, s + \Delta s) = \mathcal{T} \exp\left[-i \int_s^{s+\Delta s} \mathcal{H}(s')\mathrm{d}s'\right] \Phi(u, s), \tag{36}$$

where $\mathcal{T}$ is the time-ordering operator. Thus the task is reduced to finding a numerical approximation of the time-ordered propagator

$$U(s + \Delta s, s) = \mathcal{T} \exp\left[-i \int_s^{s+\Delta s} \mathcal{H}(s')\mathrm{d}s'\right]. \tag{37}$$

Here we will show the first- and second-order approximants of Eq. (37) as given in ref. [1]. We begin with the first order approximation

$$U_1(s + \Delta s, s) = e^{-i\Delta s B(s+\Delta s)} e^{-i\Delta s A(s+\Delta s)} + O(\Delta s). \tag{38}$$

In our case, the first operator $e^{-i\Delta s B(s+\Delta s)}$ is diagonal in the position basis and thus it's action is the direct multiplication

$$e^{-i\Delta s B(s+\Delta s)}\psi(u) = e^{-i\Delta s\left(\frac{k_0}{2}\alpha(s+\Delta s)\ddot{\alpha}(s+\Delta s)u^2 + V_0(u)\right)}\psi(u). \tag{39}$$

The second operator $e^{-i\Delta s A(s+\Delta s)}$ contains the second derivative ∂_u^2 and is diagonal in Fourier-space. Thus it's action is the direct multiplication in Fourier-space

$$e^{-i\Delta s A(s+\Delta s)}\psi(u) = e^{i\Delta s\left(2k_0\alpha^2(s+\Delta s)\right)^{-1}\partial_u^2}\psi(u) = \mathcal{FT}^{-1}\left\{e^{-i\Delta s\left(2k_0\alpha^2(s+\Delta s)\right)^{-1}k_u^2}\mathcal{FT}\left\{\psi(u)\right\}\right\}, \tag{40}$$

where $\mathcal{FT}\left\{\psi(u)\right\} = \Psi(k_u)$ is the Fourier transform. As it is well-known, the Fourier transform $\mathcal{FT}$ and it's inverse $\mathcal{FT}^{-1}$ can be implemented efficiently. In summary, the complete first order propagation-step is

$$\Phi(u, s + \Delta s) = V \cdot \mathcal{FT}^{-1}\left\{D \cdot \mathcal{FT}\left\{\Phi(u, s)\right\}\right\}, \tag{41}$$

where $\cdot$ indicates element-wise multiplication and we have introduced the abbreviations

$$V = e^{-i\Delta s\left(\frac{k_0}{2}\alpha(s+\Delta s)\ddot{\alpha}(s+\Delta s)u^2+V_0(u)\right)} \tag{42}$$

$$D = e^{-i\Delta s\left(2k_0\alpha^2(s+\Delta s)\right)^{-1}k_u^2}. \tag{43}$$

The second order approximation of the propagator is given by [1]

$$U_2(s+\Delta s, s) = e^{-\frac{i}{2}\Delta s B(s+\frac{\Delta s}{2})} e^{-i\Delta s A(s+\frac{\Delta s}{2})} e^{-\frac{i}{2}\Delta s B(s+\frac{\Delta s}{2})} + O(\Delta s^2), \tag{44}$$

which leads to the propagation step

$$\Phi(u, s+\Delta s) = \tilde{V} \cdot \mathcal{FT}^{-1}\left\{\tilde{D} \cdot \mathcal{FT}\left\{\tilde{V} \cdot \Phi(u,s)\right\}\right\}, \tag{45}$$

with

$$\tilde{V} = e^{-\frac{i}{2}\Delta s\left(\frac{k_0}{2}\alpha(s+\frac{\Delta s}{2})\ddot{\alpha}(s+\frac{\Delta s}{2})u^2+V_0(u)\right)} \tag{46}$$

$$\tilde{D} = e^{-i\Delta s\left(2k_0\alpha^2(s+\frac{\Delta s}{2})\right)^{-1}k_u^2}. \tag{47}$$

At a first glance, it appears as though the higher accuracy of the second order approximation comes at the cost of a higher computation time, since an additional multiplication of the field with $\tilde{V}$ is required. However, the computational cost can be made equal to the first order propagation step by a subtle regrouping of the operations. To see this, let us consider the first three consecutive steps

$$\Phi(u, 3\Delta s) = \underbrace{\tilde{V}_2 \cdot \mathcal{FT}^{-1}\ \tilde{D}_2 \cdot \mathcal{FT}\ \tilde{V}_2}_{\text{step 3}} \cdot \underbrace{\tilde{V}_1 \cdot \mathcal{FT}^{-1}\ \tilde{D}_1 \cdot \mathcal{FT}\ \tilde{V}_1}_{\text{step 2}} \cdot \underbrace{\tilde{V}_0 \cdot \mathcal{FT}^{-1}\ \tilde{D}_0 \cdot \mathcal{FT}\ \tilde{V}_0}_{\text{step 1}} \cdot \Phi(u,0), \tag{48}$$

where we have omitted the $\{\}$-braces for clarity. Firstly, we define the field $\tilde{\Phi}(u, n\Delta s) = \tilde{V}_n \Phi(u, n\Delta s)$ leading to

$$\tilde{\Phi}(u, 3\Delta s) = \underbrace{\tilde{V}_3 \cdot \tilde{V}_2 \cdot \mathcal{FT}^{-1}\ \tilde{D}_2 \cdot \mathcal{FT}}_{\text{new step 3}}\ \underbrace{\tilde{V}_2 \cdot \tilde{V}_1 \cdot \mathcal{FT}^{-1}\ \tilde{D}_1 \cdot \mathcal{FT}}_{\text{new step 2}}\ \underbrace{\tilde{V}_1 \cdot \tilde{V}_0 \cdot \mathcal{FT}^{-1}\ \tilde{D}_0 \cdot \mathcal{FT}}_{\text{new step 1}}\ \tilde{\Phi}(u,0). \tag{49}$$

By combining the terms $\tilde{W}_n = \tilde{V}_{n+1} \cdot \tilde{V}_n$, which can be computed in a single step by evaluating $\tilde{V}$ at the appropriate distances, we have achieved an equally fast propagation step but improved the accuracy to $O(\Delta s^2)$

$$\tilde{\Phi}(u, s+\Delta s) = \tilde{W} \cdot \mathcal{FT}^{-1}\left\{\tilde{D} \cdot \mathcal{FT}\left\{\tilde{\Phi}(u,s)\right\}\right\}, \tag{50}$$

with

$$\tilde{W} = e^{-\frac{i}{2}\Delta s\left[\frac{k_0}{2}\left(\alpha(s+\frac{3\Delta s}{2})\ddot{\alpha}(s+\frac{3\Delta s}{2})+\alpha(s+\frac{\Delta s}{2})\ddot{\alpha}(s+\frac{\Delta s}{2})\right)u^2+2V_0(u)\right]}. \tag{51}$$

Whenever we want to store the correct field we need to evaluate $\Phi(u, n\Delta s) = \tilde{V}_n^{-1}\tilde{\Phi}(u, n\Delta s)$. Of course this rearrangement of the propagation operators is only beneficial if significantly less steps are stored than actually performed in one run of the simulation.

2.3 Verification Through Comparison with Analytical Solutions of the Time-dependent Harmonic Oscillator

In order to verify our method we need a well-understood system to compare our numerical simulations to. The harmonic oscillator is the ideal candidate and, in fact, analytical solutions that include a time-dependent mass-term, $c(t)\partial_x^2$, time-dependent oscillator strength, $a(t)x^2$, as well as time-dependent mixed terms such as $b(t)(x\partial_x + \partial_x x)$, are known [2]. Here we verify our method by comparing our simulations to the known analytical solution for a time-dependent harmonic oscillator strength. In the optics language, this is equivalent to a tapered 1D GRIN medium. In other words, we consider the specific refractive index distribution

$$n(x,z)^2 = -\frac{x^2}{\alpha(z)^2 z_R^2} n_0^2 + n_0^2, \tag{52}$$

where $z_R = \frac{1}{2} w_x^2 k_0$ is the Rayleigh length and w_x is the e^{-1} beam waist which leads to the potential

$$V_0(x,z) = \frac{k_0}{2} \frac{x^2}{\alpha^2 z_R^2}. \tag{53}$$

Note that $V_0(x,z)$ has the taper property $V_0(x\alpha(z),z) = V_0(x,0)$. The paraxial equation in the normal reference frame is thus

$$i\partial_z \psi = \frac{1}{2k_0}(-i\partial_x)^2\psi + \frac{k_0}{2\alpha^2 z_R^2} x^2 \psi. \tag{54}$$

We now construct the analytical solution of Eq. (54). Following ref. [2] we can identify the functions

$$c(z) = \frac{1}{2k_0} \tag{55}$$

$$a(z) = \frac{k_0}{2\alpha^2 z_R^2}, \tag{56}$$

and we need to solve the second order differential equation

$$\ddot{g}(z) = -4c(z)a(z)g(z) = -\frac{1}{\alpha(z)^2 z_R^2} g(z), \tag{57}$$

with the initial conditions $g(0) = 1$ and $\dot{g}(0) = i/z_R$. Then the set of analytical solutions is [2]

$$\psi_n(x,z) = \frac{1}{\sqrt{n!}} \left[\frac{1}{2\pi c(0) g(z)^2 z_R}\right]^{\frac{1}{4}} \left[\frac{g^*(z)}{2g(z)}\right]^{\frac{n}{2}} \exp\left(-\frac{\dot{g}(z)}{4ic(z)g(z)} x^2\right) H_n\left(\sqrt{\frac{1}{2c(0)|g(z)|^2 z_R}}\, x\right), \tag{58}$$

where $H_n(x)$ is the Hermite polynomial. We now compare the analytical and our numerical results for a linearly-, exponentially- and oscillating-exponentially tapered GRIN medium.

2.3.1 Linear GRIN Taper

The linear GRIN taper is the simplest taper with

$$\alpha(z) = 1 - \frac{z}{z_f}, \tag{59}$$

where z_f is a parameter that controls the taper angle. For this taper function, it can be shown that the analytical solution of Eq. (57) is

$$g(z) = \frac{1}{2z_R\theta}\left(a\left(1-\frac{z}{z_f}\right)^{\frac{1+\theta}{2}} + b\left(1-\frac{z}{z_f}\right)^{\frac{1-\theta}{2}}\right), \tag{60}$$

with $\theta = \sqrt{1 - 4z_f^2/z_R^2}$, $a = \theta z_R - 2iz_f - z_R$ and $b = \theta z_R + 2iz_f + z_R$. This result enables us to construct the analytical propagation in the linearly tapered GRIN medium according to Eq. (58).

2.3.2 Exponential GRIN Taper

Another interesting taper is the exponential one

$$\alpha(z) = e^{-z/z_f}. \tag{61}$$

Here we find the analytical solution

$$g(z) = \frac{\pi z_f}{2z_R} \left(aY_0 \left(\frac{z_f}{z_R} e^{z/z_f} \right) + bJ_0 \left(\frac{z_f}{z_R} e^{z/z_f} \right) \right), \tag{62}$$

with $a = J_1 \left(\frac{z_f}{z_R} \right) + iJ_0 \left(\frac{z_f}{z_R} \right)$ and $b = -Y_1 \left(\frac{z_f}{z_R} \right) - iY_0 \left(\frac{z_f}{z_R} \right)$ and $J_n(x)$, $Y_n(x)$ are the Bessel functions of first and second kind, respectively. Again, this result enables us to construct the analytical solution using Eq. (58).

2.3.3 Oscillating Exponential GRIN Taper

Finally we consider a more exotic taper of the form

$$\alpha(z) = e^{-z/z_f}(1 + A\sin(\omega z)), \tag{63}$$

where $1 > A > 0$ is the amplitude and ω the frequency of the taper oscillation. While Eq. (58) is still the correct analytical solution, even for this exotic taper, in this case there is no analytical solution of Eq. (57). As a consequence we solve Eq. (57) numerically instead and we feed these results into the analytical solution in Eq. (58).

2.3.4 Comparison of Analytics and Simulations

Now we are in a position to compare our simulations with the previously derived analytical solutions. In Fig. (1-a) we show the tapered GRIN potentials for linear, exponential and oscillating-exponential tapers. Here we choose $w_x = 20\ \mu m$, $\lambda = 1550\ nm$, $n_0 = 1.44$, the domain length $L_x = 0.7\ mm$ and the final propagation distance $L_z = 2\ cm$, with a final taper ratio $t = 1/10$. For the linear taper this results in $z_f = L_z/(1-t) \approx 2.22\ cm$, and in $z_f = -L_z/\log(t) \approx 4.61\ cm$ for the exponential tapers. In Fig. (1-b) we show the analytical solution with order $n = 2$. For our simulations we choose the grid size $N_x = 2000$ in x-direction ($\Delta x = 0.35\ \mu m$), the step size $\Delta z = 1\ \mu m$ ($N_z = 20000$). We observe an excellent agreement with the simulations, Fig. (1-c,d). This is further corroborated in Fig. (2) where we calculated the relative numerical error

$$\epsilon^2 = \int |\psi^{(a)}(x) - \psi^{(s)}(x)|^2 \mathrm{d}x = \sum_{n=1}^{N_x} |\psi_n^{(a)} - \psi_n^{(s)}|^2 \Delta x, \tag{64}$$

as a function of the step size Δz, where ψ_n is the field at grid point with indices n and $(a), (s)$ indicates analytics and simulations respectively. Note that for the error to be accurate, care has to be exercised, so that the analytical solution is evaluated at the same physical positions corresponding to the tapered reference frame. Furthermore, it is important to note that the transverse step size is a function of z, i.e. $\Delta x = \Delta x(z = 0)\alpha(z)$.

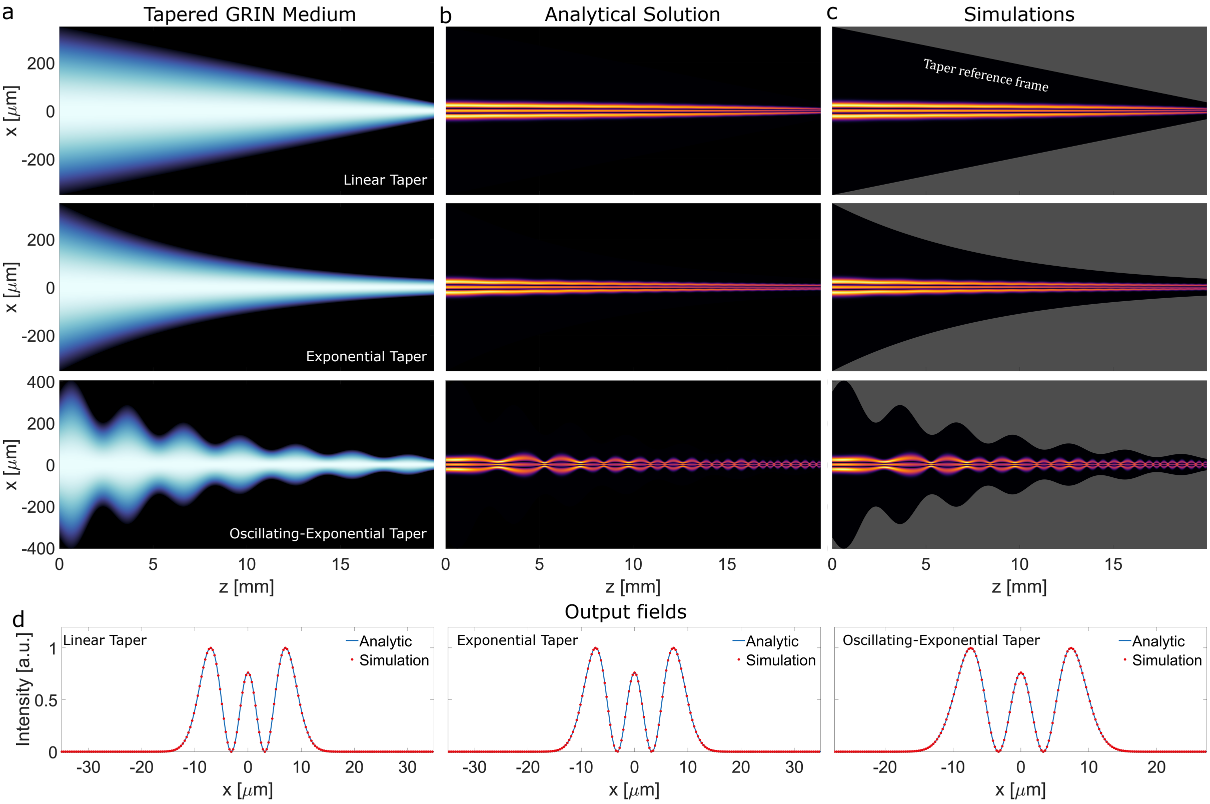

Fig. 1 Comparison of Analytical Solution and Simulations. a Tapered 1D GRIN Potential for a linear-, exponential- and oscillating-exponential taper with $n_0 = 1.44$, $w_x = 20\ \mu m$ and $\lambda = 1550\ nm$. The propagation distance is $L_z = 2\ cm$ and a final taper ratio of $t = 1/10$. **b** Analytical solutions. **c** Simulation results in the taper reference frame indicated by the black region. **d** Comparison of the final output field, where we observe an excellent match between analytics and simulations.

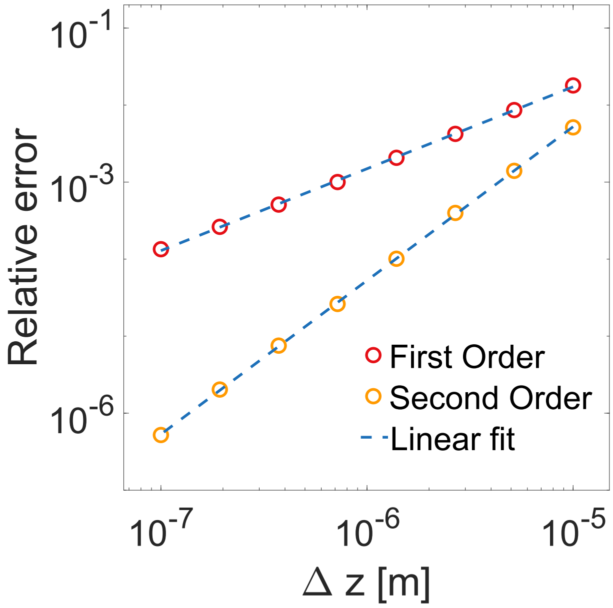

Fig. 2 Scaling of the Relative Numerical Error with the Step Size in 1D. We investigate the numerical error ϵ of our method as a function of the step-size Δz. The slopes of the linear fits are $m_1 = 1.02$ (first order propagator) and $m_2 = 1.99$ (second order propagator), as expected, showing that the second order propagator provides superior accuracy.

3 Tapered Paraxial Equation in 2D

In this section we follow the recipe outlined for the 1D tapered paraxial wave equation to obtain the corresponding 2D Fourier propagation algorithm. Furthermore, using the fact that the 2D harmonic oscillator factorizes in Cartesian coordinates, we can construct the analytical solutions for an anisotropic tapered 2D GRIN medium to compare with our method in the 2D tapered reference frame. We begin with the already derived 2D tapered paraxial equation

$$i\partial_s\psi = -\left(\frac{1}{2k_0\alpha(s)^2}\right)\nabla^2_{u,v}\psi - i\left(-\frac{\dot\alpha(s)}{\alpha(s)}\right)\left(u\partial_u + v\partial_v\right)\psi + V_0(u,v)\psi. \tag{65}$$

We use the commutation relations, $[u,\partial_u]=1$ ($[v,\partial_v]=1$), to obtain

$$i\partial_s\psi = -\left(\frac{1}{2k_0\alpha(s)^2}\right)\nabla^2_{u,v}\psi - i\left(-\frac{\dot\alpha(s)}{2\alpha(s)}\right)\left(u\partial_u + \partial_u u + v\partial_v + \partial_v v\right)\psi + i\frac{\dot\alpha(s)}{\alpha(s)}\psi + V_0(u,v)\psi. \tag{66}$$

Now we remove the extra term by defining $\phi = \alpha(s)\psi$

$$i\partial_s\phi = -\left(\frac{1}{2k_0\alpha(s)^2}\right)\nabla^2_{u,v}\phi - i\left(-\frac{\dot\alpha(s)}{2\alpha(s)}\right)\left(u\partial_u + \partial_u u + v\partial_v + \partial_v v\right)\phi + V_0(u,v)\phi. \tag{67}$$

We use the short-hand notation $c(s) = 1/(2k_0\alpha(s)^2)$, $b(s) = -\dot\alpha(s)/(2\alpha(s))$ and complete the square

$$\begin{aligned}
i\partial_s\phi &= -c(s)\left(\partial_u^2+\partial_v^2\right)\phi - ib(s)\left(u\partial_u + \partial_u u + v\partial_v + \partial_v v\right)\phi + V_0(u,v)\phi && (68)\\
&= -c(s)\left[\partial_u^2+\partial_v^2 + i\frac{b(s)}{c(s)}\left(u\partial_u + \partial_u u + v\partial_v + \partial_v v\right)\right]\phi + V_0(u,v)\phi && (69)\\
&= -c(s)\left[\left(\partial_u + i\frac{b(s)}{c(s)}u\right)^2 + \frac{b^2(s)}{c^2(s)}u^2 + \left(\partial_v + i\frac{b(s)}{c(s)}v\right)^2 + \frac{b^2(s)}{c^2(s)}v^2\right]\phi + V_0(u,v)\phi && (70)\\
&= c(s)\left(i\vec\nabla_{u,v} - \frac{b(s)}{c(s)}\vec r_{u,v}\right)^2\phi - \frac{b^2(s)}{c(s)}\left(u^2+v^2\right)\phi + V_0(u,v)\phi && (71)\\
&= c(s)\left(i\vec\nabla_{u,v} + \vec A(u,v,s)\right)^2\phi + V_1(u,v,s)\phi + V_0(u,v)\phi. && (72)
\end{aligned}$$

In the last step we have obtained the 2D tapered paraxial wave equation, which includes the vector gauge field

$$\vec A(u,v,s) = -\frac{b(s)}{c(s)}\vec r_{u,v} = k_0\alpha(s)\dot\alpha(s)\begin{pmatrix} u \\ v\end{pmatrix}, \tag{73}$$

and the new 2D harmonic oscillator potential

$$V_1(u,v,s) = -\frac{b^2(s)}{c(s)}\left(u^2+v^2\right) = -\frac{k_0}{2}\dot\alpha^2(s)\left(u^2+v^2\right). \tag{74}$$

Finally, we remove the gauge field with the transformation

$$\begin{aligned}
\phi(u,v,s) \to \Phi(u,v,s) &= e^{i\Lambda(u,v,s)}\phi(u,v,s) && (75)\\
\vec A \to \vec A' &= \vec A + \vec\nabla_{u,v}\Lambda && (76)\\
V \to V' &= V - \partial_s\Lambda && (77)
\end{aligned}$$

and choosing

$$\Lambda(u,v,s) = -\frac{k_0}{2}\alpha(s)\dot\alpha(s)(u^2+v^2). \tag{78}$$

We obtain the additional potential

$$-\partial_s \Lambda = \frac{k_0}{2}\left(\dot{\alpha}^2(s) + \alpha(s)\ddot{\alpha}(s)\right)\left(u^2+v^2\right), \tag{79}$$

and thus the final form of the 2D tapered paraxial wave equation

$$i\partial_s \Phi = -\left(\frac{1}{2k_0\alpha(s)^2}\right)\vec{\nabla}^2_{u,v}\Phi + \left(\frac{k_0}{2}\alpha(s)\ddot{\alpha}(s)\left(u^2+v^2\right) + V_0(u,v)\right)\Phi, \tag{80}$$

where the original field is acquired via

$$\psi(u,v,s) = \frac{1}{\alpha(s)} e^{i\frac{k_0}{2}\alpha(s)\dot{\alpha}(s)(u^2+v^2)}\Phi(u,v,s). \tag{81}$$

It is noteworthy that, apart from the additional dimension v, the only difference between the 1D and 2D case is the different scaling factor of $1/\sqrt{\alpha(s)}$ $(1/\alpha(s))$ in 1D (2D) to obtain the original field.

3.1 2D Fourier Propagation in the Taper Reference Frame

We can now immediately give the first and second order approximations of the propagation operator. In first order we have the propagation step

$$\Phi(u,v,s+\Delta s) = V \cdot \mathcal{FT}_2^{-1}\left\{D \cdot \mathcal{FT}_2\left\{\Phi(u,v,s)\right\}\right\}, \tag{82}$$

where $\mathcal{FT}_2\left\{\psi(u,v)\right\} = \Psi(k_u,k_v)$ is the 2D Fourier transform and

$$V = e^{-i\Delta s\left(\frac{k_0}{2}\alpha(s+\Delta s)\ddot{\alpha}(s+\Delta s)\left(u^2+v^2\right)+V_0(u,v)\right)} \tag{83}$$

$$D = e^{-i\Delta s\left(2k_0\alpha^2(s+\Delta s)\right)^{-1}\left(k_u^2+k_v^2\right)}. \tag{84}$$

Similarly we obtain the second order step

$$\tilde{\Phi}(u,v,s+\Delta s) = \tilde{W} \cdot \mathcal{FT}_2^{-1}\left\{\tilde{D} \cdot \mathcal{FT}_2\left\{\tilde{\Phi}(u,v,s)\right\}\right\}, \tag{85}$$

where $\tilde{\Phi}(u,v,s) = \tilde{V}\Phi(u,v,s)$ and

$$\tilde{V} = e^{-\frac{i}{2}\Delta s\left(\frac{k_0}{2}\alpha(s+\frac{\Delta s}{2})\ddot{\alpha}(s+\frac{\Delta s}{2})\left(u^2+v^2\right)+V_0(u,v)\right)} \tag{86}$$

$$\tilde{W} = e^{-\frac{i}{2}\Delta s\left[\frac{k_0}{2}\left(\alpha(s+\frac{3\Delta s}{2})\ddot{\alpha}(s+\frac{3\Delta s}{2})+\alpha(s+\frac{\Delta s}{2})\ddot{\alpha}(s+\frac{\Delta s}{2})\right)\left(u^2+v^2\right)+2V_0(u,v)\right]} \tag{87}$$

$$\tilde{D} = e^{-i\Delta s\left(2k_0\alpha^2(s+\frac{\Delta s}{2})\right)^{-1}\left(k_u^2+k_v^2\right)}. \tag{88}$$

3.2 Analytical Solutions for the Tapered 2D Harmonic Oscillator

To test our 2D propagation method, we derive the analytical solution of the 2D tapered GRIN medium with the refractive index distribution

$$n(x,y,z)^2 = -\frac{n_0^2}{\alpha(z)^2}\left(\frac{x^2}{z_{R_x}^2} + \frac{y^2}{z_{R_y}^2}\right) + n_0^2, \tag{89}$$

where $z_{R_x} = w_x^2 k_0/2$, $z_{R_y} = w_y^2 k_0/2$ are the Rayleigh lengths and w_x (w_y) is the e^{-1} beam waist in x-(y-)direction which leads to the potential

$$V_0(x,y,z) = \frac{k_0}{2\alpha^2(z)}\left(\frac{x^2}{z_{R_x}^2} + \frac{y^2}{z_{R_y}^2}\right). \tag{90}$$

The paraxial equation in the normal reference frame is thus

$$
\begin{aligned}
i\partial_z\psi(x,y,z) &= \frac{1}{2k_0}(-i\partial_x)^2\psi + \frac{k_0}{2\alpha^2(z)z_{R_x}^2}x^2\psi + \frac{1}{2k_0}(-i\partial_y)^2\psi + \frac{k_0}{2\alpha^2(z)z_{R_y}^2}y^2\psi && (91)\\
&= \mathcal{H}(x,y,z)\psi(x,y,z). && (92)
\end{aligned}
$$

We can group the terms on the right-hand-side into two operators that only act on functions of (x,∂_x) and (y,∂_y) respectively, i.e.

$$
\begin{aligned}
\mathcal{H}_x(x,z) &= \frac{1}{2k_0}(-i\partial_x)^2 + \frac{k_0}{2\alpha^2(z)z_{R_x}^2}x^2 && (93)\\
\mathcal{H}_y(y,z) &= \frac{1}{2k_0}(-i\partial_y)^2 + \frac{k_0}{2\alpha^2(z)z_{R_y}^2}y^2, && (94)
\end{aligned}
$$

with $\mathcal{H}(x,y,z)=\mathcal{H}_x(x,z)+\mathcal{H}_y(y,z)$. Using Eq. (58) we can construct $\psi_{n_x}(x,z)$ and $\psi_{n_y}(y,z)$ as solutions of the separate 1D equations

$$
\begin{aligned}
i\partial_z\psi_{n_x}(x,z) &= \mathcal{H}_x(z)\psi_{n_x}(x,z) && (95)\\
i\partial_z\psi_{n_y}(y,z) &= \mathcal{H}_y(z)\psi_{n_y}(y,z). && (96)
\end{aligned}
$$

Then we can find a 2D solution by simple multiplication

$$
\psi_{n_x,n_y}(x,y,z) = \psi_{n_x}(x,z)\psi_{n_y}(y,z) \tag{97}
$$

since

$$
\begin{aligned}
i\partial_z\psi_{n_x,n_y}(x,y,z) &= i\partial_z\psi_{n_x}(x,z)\psi_{n_y}(y,z) && (98)\\
&= \psi_{n_x}(x,z)\left(i\partial_z\psi_{n_y}(y,z)\right) + \psi_{n_y}(y,z)\left(i\partial_z\psi_{n_x}(x,z)\right) && (99)\\
&= \psi_{n_x}(x,z)\mathcal{H}_y(y,z)\psi_{n_y}(y,z) + \psi_{n_y}(y,z)\mathcal{H}_x(x,z)\psi_{n_x}(x,z) && (100)\\
&= \mathcal{H}_y(y,z)\psi_{n_x}(x,z)\psi_{n_y}(y,z) + \mathcal{H}_x(x,z)\psi_{n_x}(x,z)\psi_{n_y}(y,z) && (101)\\
&= \left(\mathcal{H}_x(x,z)+\mathcal{H}_y(y,z)\right)\psi_{n_x}(x,z)\psi_{n_y}(y,z) && (102)\\
&= \mathcal{H}(x,y,z)\psi_{n_x,n_y}(x,y,z). && (103)
\end{aligned}
$$

Therefore we have found our reference analytical solution for the tapered 2D GRIN medium

$$
\begin{aligned}
\psi_{n_x,n_y}(x,y,z) =& \frac{1}{\sqrt{n_x!n_y!}}\left[\frac{1}{2\pi c(0)}\right]^{\frac{1}{2}}\left[\frac{1}{g_x(z)^2g_y(z)^2z_{R_x}z_{R_y}}\right]^{\frac{1}{4}}\left[\frac{g_x^*(z)}{2g_x(z)}\right]^{\frac{n_x}{2}}\left[\frac{g_y^*(z)}{2g_y(z)}\right]^{\frac{n_y}{2}}\\
&\exp\left(-\frac{\dot g_x(z)}{4ic(z)g_x(z)}x^2\right)\exp\left(-\frac{\dot g_y(z)}{4ic(z)g_y(z)}y^2\right) \qquad (104)\\
&H_{n_x}\left(\sqrt{\frac{1}{2c(0)|g_x(z)|^2z_{R_x}}}x\right)H_{n_y}\left(\sqrt{\frac{1}{2c(0)|g_y(z)|^2z_{R_y}}}y\right),
\end{aligned}
$$

where $g_{x/y}(z)$ are the solutions of

$$
\ddot g_{x/y}(z) = -4c(z)a_{x/y}(z)g_{x/y}(z) = -\frac{1}{\alpha(z)^2z_{R_{x/y}}^2}g_{x/y}(z), \tag{105}
$$

with the initial conditions $g_{x/y}(0)=1$ and $\dot g_{x/y}(0)=i/z_{R_{x/y}}$.

3.3 Comparison of Analytics and Simulations in 2D

Now we are in a position to compare our simulations with the previously derived analytical solutions in 2D. In Fig. (3) we show the tapered 2D GRIN potentials for linear, exponential and oscillating-exponential tapers. Here we choose $w_x = 20\ \mu m$, $w_y = 15\ \mu m$, $\lambda = 1550\ nm$, $n_0 = 1.44$, the domain length $L_x = L_y = 1\ mm$ and the final propagation distance $L_z = 2\ cm$, with a final taper ratio $t = 1/10$. For the linear taper this results in $z_f = L_z/(1-t) \approx 2.22\ cm$, and in $z_f = -L_z/\log(t) \approx 4.61\ cm$ for the exponential tapers. In Fig. (4) we show the analytical solution with order $n_x = 2, n_y = 4$. For our simulations we choose the grid size $N_x = N_y = 1000$ in x-direction ($\Delta x = \Delta y = 1\ \mu m$), the step size $\Delta z = 1\ \mu m$ ($N_z = 20000$). We observe an excellent agreement between the analytical solutions and the simulations in Fig. (4). This is further corroborated in Fig. (5) where we calculated the relative numerical error

$$\epsilon^2 = \sum_{n,m=1}^{N_x,N_y} |\psi^{(a)}_{n,m} - \psi^{(s)}_{n,m}|^2 \Delta x \Delta y, \tag{106}$$

as a function of the step size, where $\psi_{n,m}$ is the field at grid point with indices n, m and $(a), (s)$ indicates analytical and simulation results respectively. Note that care has to be exercised, so that the analytical solution is evaluated at the same physical positions corresponding to the tapered reference frame. Furthermore, it is important to note that the transverse step size is a function of z, i.e. $\Delta x = \Delta x(z = 0)\alpha(z)$.

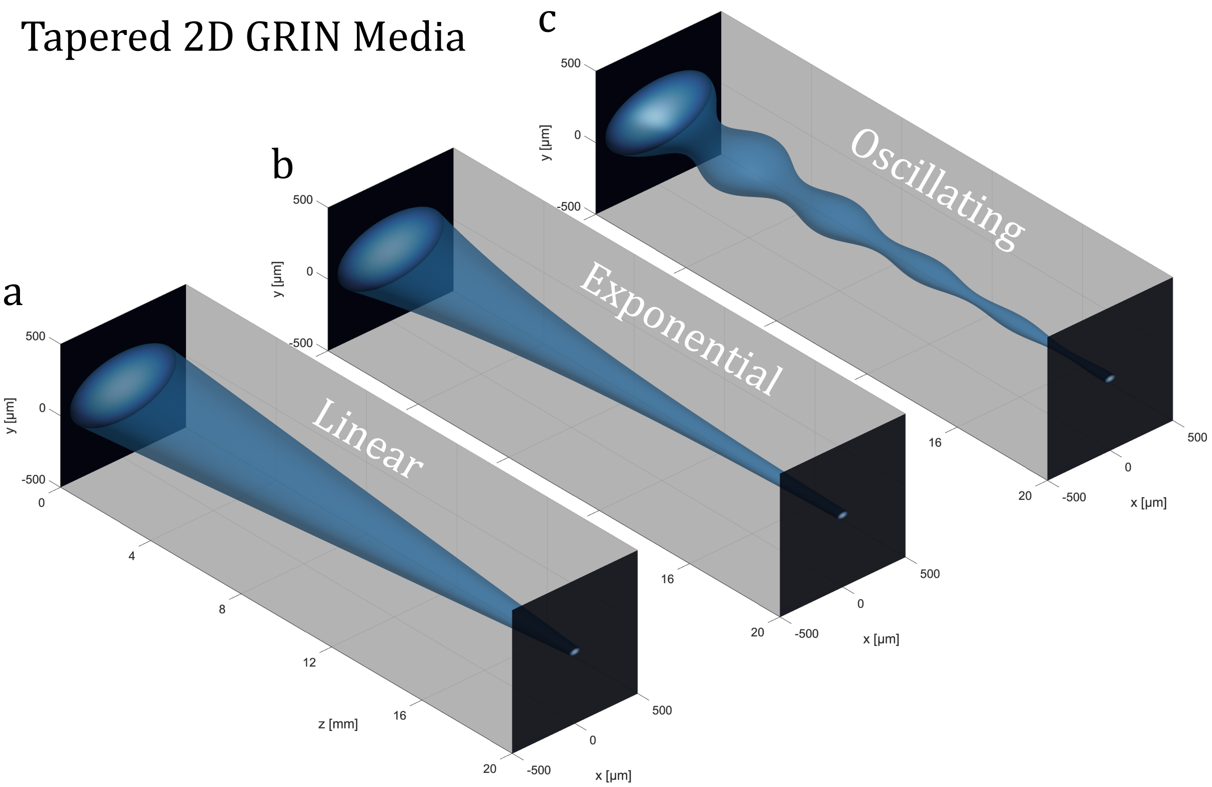

Fig. 3 Tapered 2D GRIN Potentials. We show a 3D plot of the tapered GRIN media refractive index distribution $n(x, y, z)^2$, for **a** linear-, **b** exponential- and **c** oscillating-exponential taper. We choose $n_0 = 1.44$, $w_x = 20\ \mu m$, $w_y = 15\ \mu m$ and $\lambda = 1550\ nm$. The propagation distance is $L_z = 2\ cm$ with final taper ratio of $t = 1/10$. The light blue surface indicates the iso-surface where the refractive index is $n(x, y, z)^2 = 1.8$.

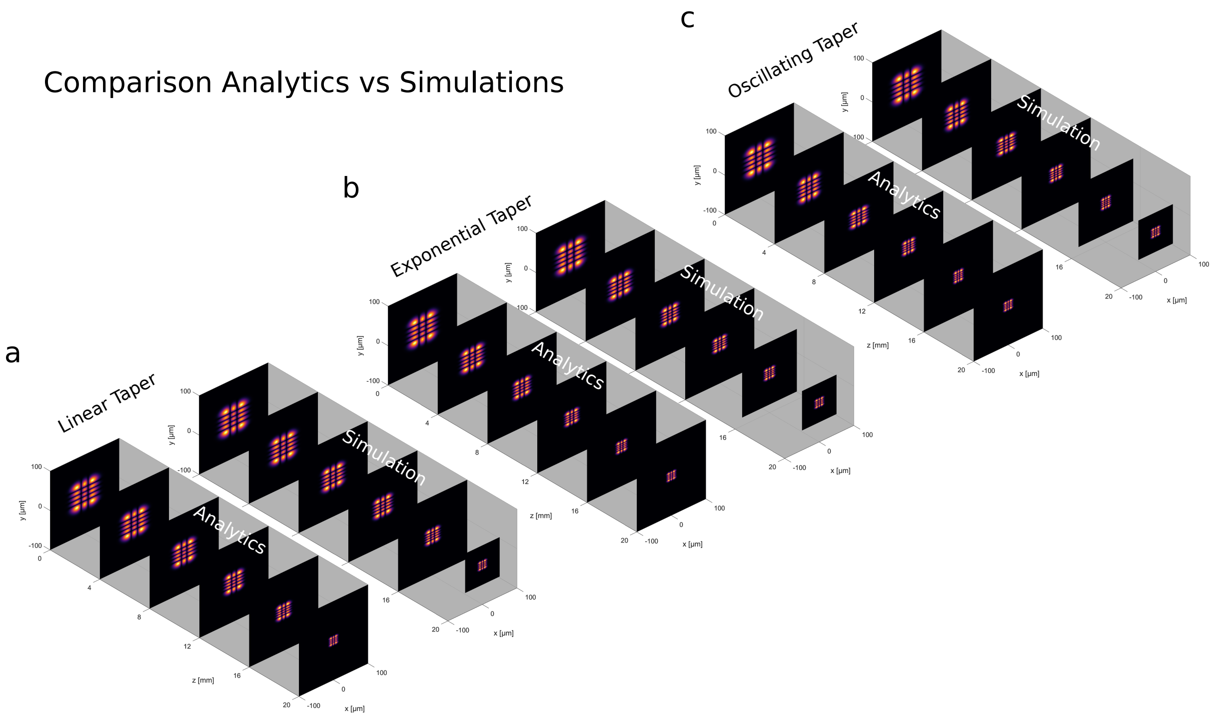

Fig. 4 Comparison of Analytical Solutions and Simulations. We show the propagation of the $n_x = 2, n_y = 4$ analytical solution and the corresponding simulation in the taper reference frame for **a** linear-, **b** exponential- and **c** oscillating-exponential taper. We observe an excellent agreement in all cases.

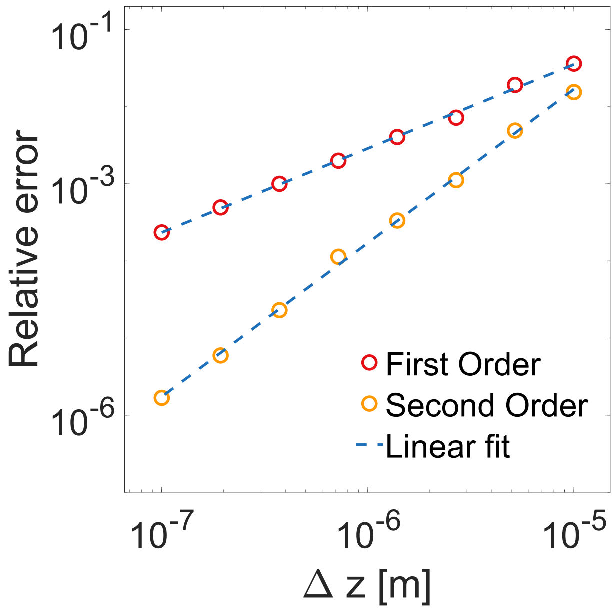

Fig. 5 Scaling of the Relative Numerical Error with the Step Size in 2D. We investigate the numerical error ϵ of our method as a function of the step-size Δz. The slopes of the linear fits are $m_1 = 1.08$ (first order propagator) and $m_2 = 1.99$ (second order propagator), as expected, showing that the second order propagator provides superior accuracy.

4 Comparison of Standard Fourier Propagation versus Tapered Fourier Propagation in 2D GRIN Media

In this section we highlight the advantages of our method compared to the standard Fourier propagation method. We first establish the standard 2D Fourier propagation method, which directly solves the paraxial equation in normal (untapered) coordinates

$$i\partial_z\psi = -\left(\frac{1}{2k_0}\right)\vec{\nabla}^2_{x,y}\psi + V_0(x,y,z)\psi. \tag{107}$$

The second order propagation step is then

$$\tilde{\psi}(x,y,z+\Delta z) = \tilde{W}\cdot\mathcal{FT}_2^{-1}\left\{\tilde{D}\cdot\mathcal{FT}_2\left\{\tilde{\psi}(x,y,z)\right\}\right\}, \tag{108}$$

where $\tilde{\psi}(x,y,z) = \tilde{V}\psi(x,y,z)$ and

$$\tilde{V} = e^{-\frac{i}{2}\Delta z V_0(x,y,z+\frac{\Delta z}{2})} \tag{109}$$

$$\tilde{W} = e^{-\frac{i}{2}\Delta z\left(V_0(x,y,z+\frac{3\Delta z}{2})+V_0(x,y,z+\frac{\Delta z}{2})\right)} \tag{110}$$

$$\tilde{D} = e^{-i\Delta z\frac{1}{2k_0}\left(k_x^2+k_y^2\right)}. \tag{111}$$

Thus, in this method it is necessary to obtain the new optical potential at every time step. The naive way - and computationally most demanding one - is to obtain the new potential by a full recalculation, where all relevant distances are replaced by the tapered distances, which we term the "Recalculate"-method. As an alternative way we use the built-in Matlab function *imwarp*() to obtain the shrunk version of the initial potential $V_0(x,y,0)$, which we call the "Resize"-method.

We now compare our method ("Taper"-method) and the two standard methods in a tapered 2D GRIN medium. Here we choose $w_x = 20\ \mu m$, $w_y = 15\ \mu m$, $\lambda = 1550\ nm$, $n_0 = 1.44$, the domain length $L_x = L_y = 4\ mm$ and the final propagation distance $L_z = 2\ cm$. As the taper function we choose the challenging oscillating taper $\alpha(z) = \exp(-z/z_f)(3/4 + 1/4\cos(2\pi z/(Lz/5)))$ with a final taper ratio $t = 1/10$. This results in $z_f = -L_z/\log(t) \approx 0.87\ cm$. In Fig. (6-a) we observe the expected Δz^2 scaling of the taper method. The recalculate method saturates at $\Delta z \approx 1\ \mu m$ due to the discretization error in the transverse directions. The resize method completely fails in this regime, since the resized potential is filled with a constant value outside the original potential, which introduces significant errors in addition to the discretization error. In the same fashion we observe in Fig. (6-b) that our method saturates much earlier (for larger Δx) than the standard methods, which is a significant advantage. The recalculate method requires a much finer grid in order to saturate at the Δz-discretization error. Again, the resize method fails completely in the 2D GRIN medium. Lastly, we have measured the computation times per propagation step in Fig. (6-c) and we see again a significant advantage for our method. In summary the taper reference frame approach produces more accurate results in less computational time. In the next section we highlight the resolution advantage of our method.

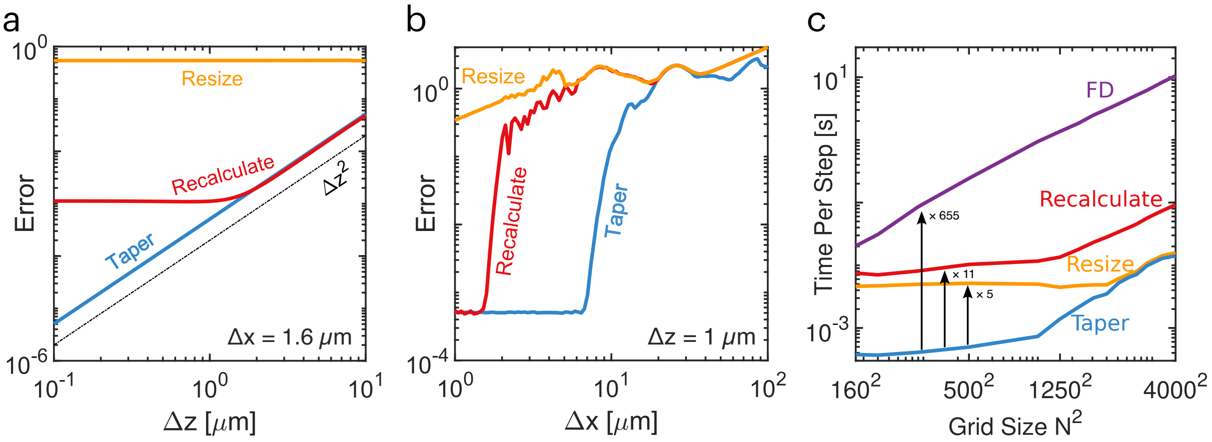

Fig. 6 Comparative Analysis of Accuracy and Speed - Standard Methods versus Taper Reference Frame Method. **a** Scaling of the error as a function of the propagation step size, Δz, in a tapered 2D-GRIN medium, with transverse resolution $\Delta x = \Delta y = 1.6\ \mu m$. We show the resize method (orange), the recalculate method (red) and our taper method (blue). The dotted black line indicates the expected Δz^2 scaling of the three-step Fourier method. **b** Error of the standard method (resize and recalculate) and our method (taper) in a tapered 2D-GRIN medium as a function of the transverse step size $\Delta x = \Delta y$, with propagation step-size $\Delta z = 1\ \mu m$. **c** Computation times for a full propagation step for each method for various $N \times N$ transverse numerical grid sizes. Additionally, we show the performance of a commercial Finite Difference (FD) beam propagation method in a comparable 4-core lantern.

5 Comparison of Taper Method to Standard Methods in a Photonic Lantern

To test our new method and compare it with the standard approach, we replicated the results from Ref. [3], where the authors used a hybrid mode-selective photonic lantern to optimize broadband starlight injection into a single-mode fiber. This photonic lantern consists of an array of 19 single-mode fibers arranged in a hexagonal pattern at the untapered output facet, also known as the multi-core face, as shown on the left side of Fig. (7). This array is tapered down by a factor of 10 over a length of 4 cm, forming the multimode input facet of the lantern, as illustrated on the right side of Fig. (7).

A unique feature of this fiber is that the central core at the single-mode multi-core output facet has a larger diameter, which allows for broadband mode selectivity for the fundamental mode of the multimode input facet. This design ensures that maximum light is directed to the science channel across a broad bandwidth [3]. The other 18 cores have the same, smaller core diameter. To maintain adiabaticity, the parameters of the multimode facet are designed to support exactly 19 spatial modes, corresponding to the 19 single-mode outputs. Due to its tapered geometry, this photonic lantern efficiently couples broadband starlight from its multimode input facet into a set of single-mode outputs. The non-mode-selective outputs are utilized for wavefront sensing, while the mode-selective output is directed to a spectrograph or another scientific instrument [3].

Figure (8-a) shows the input transverse refractive index profile of this lantern, and the relevant parameters are listed in Table (1). In our simulations, we model the cores as flat-top waveguides that support LP modes. We excite a single outer core with the fundamental LP mode and linearly taper the photonic lantern to one-tenth of its original width over a taper length of 4 cm, as depicted in Fig. (7). The resulting fields at various slices along the propagation, using the three methods (taper, resize and recalculate methods), are shown in Fig. (8-b,c,d), respectively. For a clearer comparison, Fig. (8) magnifies the region of interest, revealing significant differences in the resolution, shape, and magnitude of the output modes.

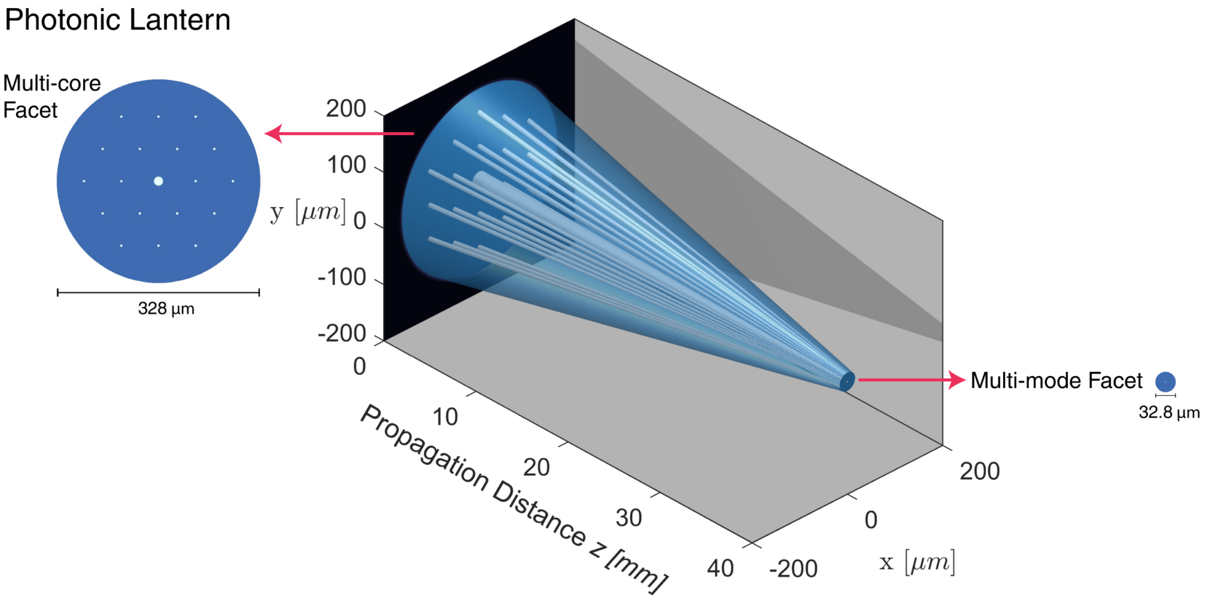

Fig. 7 Hybrid Mode-selective Photonic Lantern. Illustration of a hybrid mode-selective photonic lantern [3], created by linearly tapering down a multi-core facet with 19-cores (left) to 1/10th of its initial width, over a distance of 4 cm along the propagation distance (z-axis), transforming into a multi-mode facet (right).

Parameter	Value
Cladding n_{CL}	1.43451
Fiber n_{MC}	1.44
Ref. index n_0	1.44
Core n_C	1.4468
Fiber radius r_F	164 μm
Main core radius r_M	7.5 μm
Small Core radius r_C	2 μm
Distance Cores d	60 μm

Table 1 Photonic Lantern Parameters The relevant parameters of our test-case photonic lantern [3] shown in Fig. (8).

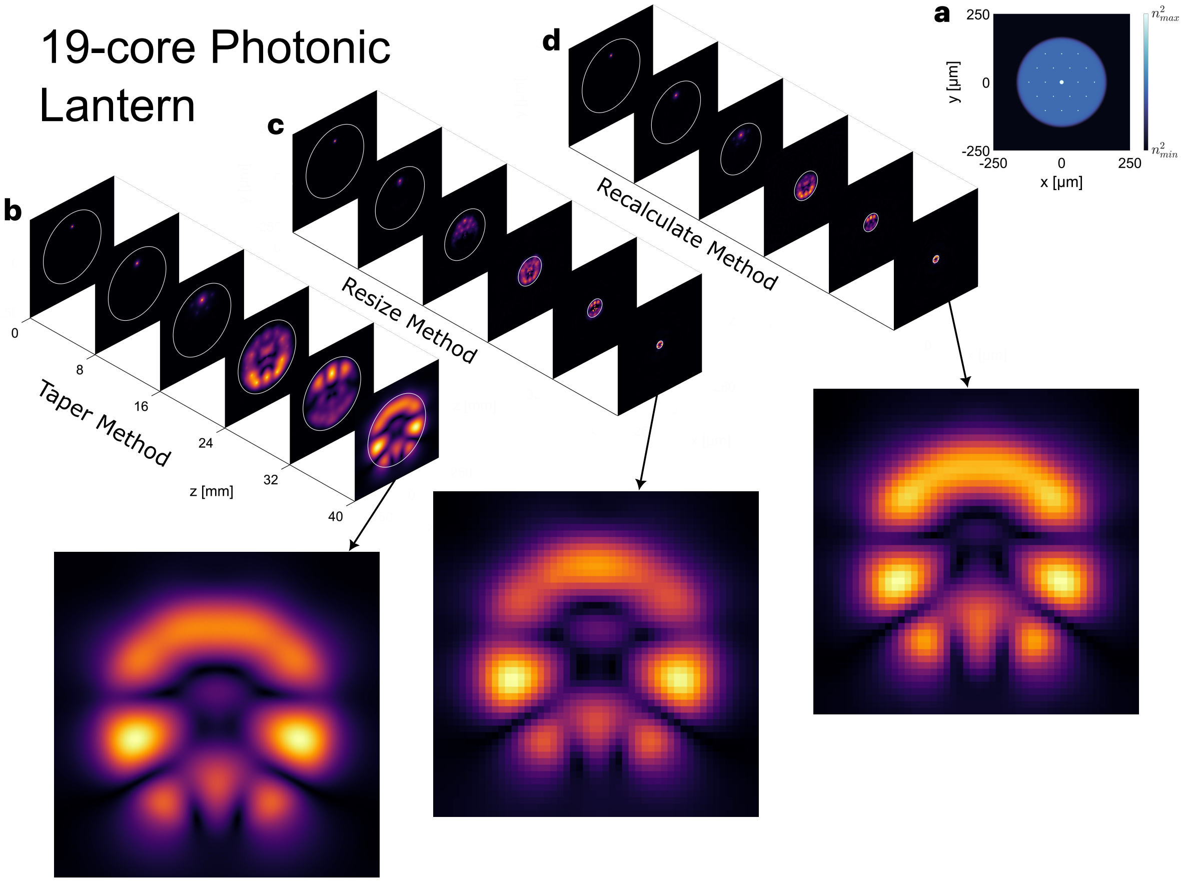

Fig. 8 Photonic lantern propagation with different numerical methods. We simulate the light propagation in a photonic lantern, with the refractive index profile shown in **a**. **b** Taper method, **c** standard resize method and the **d** standard recalculate method.

References

[1] Hatano, N., Suzuki, M.: In: Das, A., K. Chakrabarti, B. (eds.) Finding Exponential Product Formulas of Higher Orders, pp. 37–68. Springer, Berlin, Heidelberg (2005). https://doi.org/10.1007/11526216_2 . https://doi.org/10.1007/11526216_2

[2] Harari, G., Ben-Aryeh, Y., Mann, A.: Propagator for the general time-dependent harmonic oscillator with application to an ion trap. Phys. Rev. A **84**, 062104 (2011) https://doi.org/10.1103/PhysRevA.84.062104

[3] Norris, B., Betters, C., Wei, J., Yerolatsitis, S., Amezcua-Correa, R., Leon-Saval, S.: Optimal broadband starlight injection into a single-mode fibre with integrated photonic wavefront sensing. Opt. Express **30**(19), 34908–34917 (2022) https://doi.org/10.1364/OE.465639